# Spontaneous Insertion of Carbon Nanotube Bundles inside Biomembranes: a Hybrid Particle-Field Coarse-Grained Molecular Dynamics Study

*Edita Sarukhanyan*[a,b,§], *Antonio De Nicola*[a,c,§], *Danilo Roccatano,*[b] *Toshihiro Kawakatsu,*[d] *Giuseppe Milano*[a,c*]

[a)] Dipartimento di Chimica e Biologia Università di Salerno, I-84084 via Ponte don Melillo, Fisciano (SA), Italy.

[b)] Jacobs University Bremen, Campus Ring 1, D-28759, Germany.

[c)] IMAST Scarl-Technological District in Polymer and Composite Engineering, P.le Bovio 22, 80133 Napoli (NA), Italy.

[d)] Department of Physics, Tohoku University, Aoba, Aramaki, Aoba-ku, Sendai 980-8578, Japan.

§ Both of these authors contributed equally to this work.

*Corresponding-Author: gmilano@unisa.it

## ABSTRACT

The processes of CNTs bundle formation and insertion/rearrangement inside lipid bilayers, as models of cellular membranes, is described and analyzed in details using simulations on the microsecond scale. Molecular Dynamics simulations employing hybrid particle-field models (MD-SCF) show that during the insertion process lipid molecules coat bundles surfaces The distortions of bilayers are more pronounced for systems undergoing to insertion of bundles made of longer CNTs. Interestingly, in this case, for the insertion of bundles in perpendicular orientation, it has been possible to observe, for the first time, a transient poration of the bilayer and a subsequent water percolation through it.

## 1. INTRODUCTION

Due to their ability to cross cellular membranes, carbon nanotubes (CNTs) have been proposed to be exploited as nano-transporters for drugs or other biologically active molecules inside the cell[1]. After being discovered, CNTs have attracted scientific attention due to their outstanding properties and characteristics[1]. Indeed, their ability to cross cell membranes[2] opens innumerable possibilities for biomedical applications[3,4]. Their large surface area allows attachment (of chemical or physical nature) of drug molecules[5-7] and the empty core of the CNTs provides an opportunity to exploit them as nano-containers for drug[8,9] or any desired biologically active molecule encapsulation[10,11]. For this reason, several experimental studies have been performed in order to understand the pathways of internalization[12-19]. Al-Jamal et al.[12] have studied the cellular mechanism of functionalized Multi Walled CNTs (MWCNTs) by 3D electron tomography imaging. Two types of cells – epithelial lung carcinoma cells (A549) and human monocyte-derived macrophages (HMMs) have been considered for the interactions with $NH^{3+}$ functionalized MWCNTs. The results of the study suggest that the CNT internalizations can occur either by direct piercing of the membrane of single nanotubes or by the wrapping of the nanotube by lipids of the cell membrane[12]. The study of the mechanism of uptake of single walled CNTs (SWCNTs) by HMMs has been performed by Porter et al.[14] using confocal microscopy and transmission electron microscopy (TME) techniques. This study suggested endocytosis and passive diffusion as possible mechanism. However, in a different study by Yaron[19] and coworkers based on confocal Raman spectroscopy and fluorescence lifetime imaging (FLIM) have found that the internalization of SWCNT occurs by only endocytosis and not for passive diffusion through membrane. The SWCNTs used in all this

studies were non covalently functionalized by Pluronic F127 (PF-127). It was found that PF-127-SWCNT were localized in endosomes while interacting with HeLa cells[1,20].

A molecular understanding of the mechanism of interaction of carbon CNTs with cellular membranes would help the development of CNTs based systems for targeted drug delivery. So far, experimental methods can provide for these systems only limited information at the molecular scale level. For this reason, several simulation studies involving CNT and lipid bilayers have been reported[17,18,21-27]. On the contrary, molecular dynamics simulations based on atomistic or coarse-grained models can provide detailed information on these processes. Unfortunately, the processes of insertion and rearrangement even of a single CNT into a lipid bilayer are slow if compared whit the timescales reachable by atomistic simulations. For this reason, often special techniques (biased simulations such as steered molecular dynamics or free energy scans along a given reaction coordinate) aimed to explore this process are needed. Atomistic simulations have been employed to perform steered molecular dynamics (SMD)[17] and static scans of environmental free energy[18] to study the insertion of very short (typical lengths were 2 nm ref. [17] and from 3 to 6 nm ref [18]) single CNTs into a lipid bilayer. Parthasarathi et al. built up atomistic models where CNTs are embedded in the lipid bilayer from the beginning of the simulations and investigated perturbations caused by the presence of single CNTs and their bundles (having CNTs length of 6 nm) on a lipid bilayer[21]. Moreover, the insertion process of a small graphene nanosheet into a lipid bilayer structure has been studied using atomistic simulations[22].

In order to explore length and time scales relevant to these problems, a number of simulation studies using coarse-grained (GC) models have been used proposed to characterize the process of spontaneous insertion of several nanosized objects into lipid bilayers. In particular, hydrophobic

nanopores[23], fullerenes[24,25], SWCNT[18], and the piercing mechanism of a single CNT into a model membrane[26] have been studies using CG models. The mechanism of spontaneous insertion of short pristine CNTs has been recently studied by Sansom et. al using molecular dynamics simulations of CG models[27]. In particular, in this study the spontaneous insertion of single CNTs of different types (single and multi-walled) and sizes (length ranging from 2 to 10 nm) inside model membranes has been characterized. Baoukina et al. studied using CG models the insertion of single CNTs and bundles formed by short CNTs (having lengths up to 6.5 nm) by molecular dynamics simulations[28].

Whit these precedents, the aim of the present paper is to characterize the insertion mechanism of bundles formed by aggregation of CNTs of different lengths (ranging from 4 to 20 nm). The relevance of these systems is related to the main difficulty in the use of CNT in nanomedicine associated with their hydrophobicity and tendency to aggregate into bundles. In fact, for practical applications, such aggregates have cytotoxic effect and even cause cell death in dose dependent manner[29]. Systems size and simulations timescales suitable to treat and to observe the spontaneous insertion process of CNTs bundles can be still feasible for coarse-grained models still close to atomistic (typically one bead corresponds to four non hydrogen atoms, 4:1 mapping), as the ones reported in this paper, if non-bonded interactions are treated using a Self Consistent Field (SCF) theory approach having models based on a hybrid particle-field (PF) representation[30].

The paper is organized as follows, in the section models and methods, the simulation methodology based on MD and hybrid PF representation is briefly introduced and the models used in the present paper are described. In the results and discussion section the process of CNTs

bundle formation is described and then the process of insertion and rearrangement of bundles formed by CNTs of length ranging from 4 to 20 nm is described and analyzed in details.

## 2. MODELS AND METHODS

### *2.1 Simulation Methodology*

The simulations reported in this paper have been performed using a hybrid particle-field scheme combining Molecular Dynamics (MD) and Self Consistent Field theory.

These hybrid approach, due to its computational efficiency, is gaining popularity for simulations of several soft matter systems including nanocomposites[31] and biomembranes[32-35]. Particle and field representations of coarse-grained models of homopolymer and block copolymer systems have been used in the single chain in mean field (SCMF) method introduces by Muller *et al*.[36,37]. More recently, the MD method has been combined with SCF description, which hereafter we call "MD-SCF" approach. In particular, an implementation suitable for the treatment of atomistic force fields and/or specific CG models has been reported and validated[30,38].

The coarse-grained models adopted in this study for lipids have been extensively described and validated in two previous papers[39,40] and recently reviewed in the framework of efficient strategies for biomembranes modelling[33]. The main advantage of hybrid MD-SCF scheme is that the most computationally expensive part of the MD simulations, i.e. the evaluation of the non-bonded force between atoms of different molecules, is replaced by the evaluation of forces between independent molecules with an external potential. The external potential $V(\mathbf{r})$, calculated from the values of the density at position $\mathbf{r}$ is:

$$V_K(\mathbf{r}) = \frac{\delta W\left[\{\phi_K(\mathbf{r})\}\right]}{\delta \phi_K(\mathbf{r})} = k_B T \sum_{K'} \chi_{KK'} \phi_{K'}(\mathbf{r}) + \frac{1}{\kappa}\left(\sum_K \phi_K(\mathbf{r}) - 1\right). \qquad (1)$$

a derivation of eq. (1) and the approximations behind it are reported in the supporting information section. The first addend of eq. (1) corresponds to the interaction of a single particle of type *K* with the fields due to particles of type *K*'. The second addend is the so-called incompressibility condition keeping the density homogenous in the space.

In order to connect particle and field models, for the proposed hybrid MD-SCF scheme, it is necessary to obtain a smooth coarse-grained density function directly from the particle positions. This function is obtained by implementing a mesh based approach which is suitable to obtain also the density derivatives needed to calculate forces. The details of the implementation of this approach and a complete derivation is reported in references[30,38]. In order to help the reader, in the supporting information section a brief overview of the theoretical scheme and its implementation is included.

*2.2 Simulation Details*

Simulations reported here have been performed using the parallelized version of the OCCAM code[41]. The compositions of each simulated system are reported in Table 1.

All simulations have been performed with velocity Verlet algorithm using a time step of 0.03 ps in the *NVT* ensemble by keeping the temperature constant at 325 K using Andersen thermostat with a collision frequency of 5 $ps^{-1}$. The calculations of the fields have been performed using a grid with a resolution of 0.705 nm and an update frequency of 300 steps. This choice of the grid size guarantees good reproduction of lipid properties[39,40]. Furthermore the value 0.705 nm is almost half of the CNTs diameters, in this way excluded volume interactions between CNTs is properly described by the incompressibility condition (second addend of eq. 1).

## 3. Results and Discussion

### *3.1 Bundle formation*

A system of six nanotubes of length 4.7 nm in water has been simulated (system I in Tab. 1) . The initial configuration was made by placing CNTs randomly in the simulation box, but avoiding overlapping between them, and, hence by adding water beads. In Figure 1, together with the behavior of the particle-field potential (the first addend of eq. 2) several snapshots are shown. A first sudden aggregation, corresponding to a drop in the particle-field potential, between closest CNTs is obtained. The first snapshots of Figure 1 show some disordered aggregations between two or three CNTs. In particular, unstable (small contact surface) and stable (large contact surface) pairs between CNTs can be identified. During the simulation it is possible to observe unstable pairs dissociating or evolving through stable pairs. Stable pairs, when formed, are able to promote aggregation of further CNTs until, in almost 250 ns, an ordered bundle is formed. It is interesting to see that when stable contacts are formed and contemporary dissociations or other pairs do not occur this corresponds to fast drops in the particle-field potential (for instance from the second to the third configuration of Figure 1).

Larger bundle or bundles having longer CNTs show similar behaviors to the ones reported here. Ordered bundles configurations employed in the simulations of the next sections for systems having CNTs long 10 and 20 nm (systems III and IV) have been constructed from the beginning of the simulation and equilibrated in water.

### *3.2 Bundles Insertion into Lipid Bilayers*

In Figure 3A the time behavior of the center of mass position and orientation of a bundle of six CNTs with length 4.6 nm are reported. In particular, for the system II in Figure 3, and for all the other systems reported in the present paper, the position along the *Z* axis of the center of mass of

the bundle is reported considering as origin the average *Z* coordinate of phospholipids in the first layer. The orientation of the CNT bundle, as schematized in Figure 2, is calculated considering the angle of the bundle axis with respect to the *z* direction perpendicular to the bilayer plane. In particular, the order parameter $P_2(t)$ has been calculated from the second order Legendre polynomial $P_2(t) = \frac{3}{2}\cos^2(\theta(t)) - \frac{1}{2}$. Values of $P_2$ close to unity indicate parallel or antiparallel orientations; values close to -0.5 indicate a perpendicular orientation.

As shown in Figure 3A, from the beginning of the MD simulation there is a decrease of the CNT height toward the hydrophobic region of the lipid bilayer. In particular, after about 120 ns the insertion of the CNT bundle inside the hydrophobic region is completed. As shown in Figure 3C, there is no strong correlation between CNT height with respect to the lipid bilayer and its orientation. Due to the low aspect ratio of the CNTs (their length is 4.6 nm) the orientation of the CNT bundle is very variable. ~~-~~ During the simulation the intermolecular potential reported in Figure 3B (first addend of eq. 1 in the particle-field approximation) shows a fast and monotonic decrease up to 150 ns. These results are consistent with the ones obtained by Sansom et al. for short single CNTs inserting into lipid bilayers[27].

In order to analyze the distortions of the lipid bilayer during the insertion process, two geometrical quantities have been considered. In particular, the deviation from the equilibrium lipid height ($\Delta z$) and the value of the cosine of the angle $\theta$ between the lipid and the *z* axis as defined in Figure 2B are considered. In Figures 3D the deviation from the equilibrium height for upper (top panel of Figure 3D) and lower layers of lipids (bottom panel of Figure 3D) and the orientation of DPPC molecules with respect to the *z* axis in the upper (top of panel of Figure 3E) and lower layers (bottom of panel of Figure 3E), as defined in Figure 2B, are reported for

different configurations. In the center the corresponding configurations of CNT bundle are depicted in Figures 3D. As shown in the plots of Figure 3D, the larger perturbation on the lipids height on both upper and lower layers is obtained between 105 and 118 ns, during the insertion process of the CNT bundle with a deviation in the lipids height between 1 and 1.5 nm. This behavior becomes clearer by comparing the plots of Figure 3D and the simulation snapshots reported in Figure 3C. A similar behavior is obtained for the lipids orientation, in particular, as shown in Figures 3E in the upper layer in a region localized close to the CNT bundle, for configurations between 118 and 150 ns, where the lipid orientation is about 90° with respect to the *z* axis. When the CNT bundle approaches the lipid bilayer large distortion of the lipids heights and orientation occurs. The lipids closer to the CNTs of the bundles tend to be adsorbed on the CNT surface and to orient pointing the hydrophobic carbon tails towards and to expose the polar heads to the water phase. As shown in the following, this is a common process in all the considered systems. A schematization of this behavior is depicted in Figure 4.

In the following, simulation results involving four systems having CNT bundles of larger aspect ratios are reported. In particular, the insertions of bundles made of CNT of length 10 and 20 nm starting from parallel and perpendicular orientations of the bundle axis with respect to the bilayer plane have been simulated.

In Figure 5 the main features of the insertion process bundles made of CNTs of length 10 (system III) and 20 nm (system IV) in parallel orientation are summarized. Similarly to the system with shorter CNTs, from the beginning of the MD simulation there is a decrease of the CNT height toward the hydrophobic region of the lipid bilayer. Differently from the system with shorter CNTs, where basically no correlation between bundle height and its orientation is found, here a parallel orientation with some deviations larger for the system with CNTs of length 10 nm

(Figure 5C) and very small for the systems with CNTs of length 20 nm (Figure 5F). In both cases, during the simulation the intermolecular potential (first addend of eq. 1 in the particle-field approximation) shows a fast and monotonic decrease. The position of the CNT center of mass shows the same behavior and reaches the equilibrium value at ~ -2 nm (i.e. in the central part of the lipid bilayer, the DPPC bilayer thickness is ~ 4 nm) in about 50 ns for the bundle having CNTs long 10 nm (Figure 5A) and about 200 ns for the bundle having longer CNTs (20 nm, Figure 5D). In the Figure 6 the distortion of the height and orientation of the lipids for different snapshots taken during the insertion process of the systems III and IV are reported. For both systems, the distortion of equilibrium height of lipids is larger than the one obtained for system II having shorter CNTs (4.6 nm). In particular, for system III in the snapshot showing larger values of $\Delta z$ (Figure 6A, plot at 21 ns) there is a small region with values larger than 2 nm. The insertion process of for system IV causes larger values of $\Delta z$, in particular, in the snapshot showing larger deviations (Figure 6C, plot at 83 ns) there is an extended region having distortions going from 2 up to 3 nm.

Similar is the behavior of lipid orientation during the insertion process. Also in this case both systems III and IV are more perturbed with respect to the one with shorter CNTs, in particular, the region where the orientation is almost perpendicular is larger with a central part where the average value of the $\cos\theta$ is zero.

In Figure 7 the insertion process bundles made of CNTs of length 10 (system III) and 20 nm (system IV) in perpendicular orientation is summarized. Although the process is slower, also in this case, it is possible to observe spontaneous insertion. Comparing the plots of Figure 7C (system III) and Figure 7F (system IV) and the snapshots reported in them it is possible to

observe that, for both CNTs lengths, the insertion involves mechanism a concerted insertion/rotation of the bundle. The perturbation of both lipid heights with a region with $\Delta z$ from 1 to 3 nm for the system having CNTs long 10 nm (Figure 8A), and from 1 to 6 nm for the system having CNTs long 20 nm (Figure 8C), and orientation (strong perpendicular orientation, Figures 8B and 8D) is more localized but stronger than the one obtained with the bundles in parallel orientation.

The insertion process involving a CNT bundle in perpendicular orientation is the one showing the largest perturbation on the structure of the lipid bilayer for both system III and system IV. Moreover, in these cases, the range of perturbation is larger; in particular, large deviations of lipid height are obtained also for the lower lipid layers. An interesting aspect, due to this feature, is the formation of a transient pore in the lipid bilayers during the insertion process of the CNT bundles . In particular, as shown in Figure 9A (system III) and 9C (system IV), starting from the configuration at about 20 (for system III) and 120 ns (system IV) a poration inside the bilayer can be observed. In the Figure 9 water beads are reported in yellow. Moreover, in the Figures 9 snapshots corresponding to the maximum size of the pore (at 122 and 145 ns for systems III and IV, respectively) are also reported. It is worth noting that, differently from the other systems considered here, in this case of the insertion in perpendicular orientation for system IV, the intermolecular interactions (see the behavior of particle-field potential reported in Figures 7B and 7E) do not show a monotonic decrease, but between 100 and 200 ns shows a local maximum. Interestingly, for this system, the simulation time where the pore size is larger corresponds to the maximum of particle-field potential (see Figure 7C). In the Figures 9B and 9D the structures of the water pore and the arrangement of lipids on the CNTs surface and around the pore percolated by water is highlighted. In particular, the arrangement on CNT

surface is typical of phospholipids at low concentration in water (micellar phases), while the ones around the pore inside the hydrophobic region of the bilayer are closer to the one obtained at high lipid concentration (reverse micelles) having lipids forming reverse micelles with water inside. Moreover, snapshots showing the coating process of lipids toward the CNT surfaces are reported in Figure 2 of the supporting material.

## 4. CONCLUSIONS

In all considered systems it has been possible to observe spontaneous insertion of bundles made of CNTs of different lengths ranging from 4.6 to 20 nm. In all cases the insertion process causes distortions in both lipid height and orientation. In particular, during the insertion process lipid molecules tend to coat bundles surfaces and this causes an increase of the average lipids heights in both upper and lower lipid layers. The lipids closer to the bundle tend to orient their carbon tails toward the hydrophobic surfaces of CNTs. These distortions are more pronounced for systems having long CNTs and oriented perpendicularly to the bilayer surfaces. In all cases these distortions are transient and they become minimal when the CNTs forming the bundle rearrange inside the hydrophobic region of the lipid bilayers. Interestingly, in the case of the bundles made of CNTs long 10 and 20 nm it has been possible to observe a transient poration and a subsequent water percolation through the bilayer.

**ACKNOWLEDGMENTS**

G.M. thanks MIUR (FIRB "RETE ITALNANONET") for financial support and the HPC team of Enea (www.enea.it) for using the ENEA-GRID and the HPC facilities CRESCO (www.cresco.enea.it) in Portici.

REFERENCES

[1] L. Lacerda, A. Bianco, M. Prato, K. Kostarelos, Advanced Drug Delivery Reviews 58 (2006) 1460.
[2] K. Kostarelos, L. Lacerda, G. Pastorin, W. Wu, WieckowskiSebastien, J. Luangsivilay, S. Godefroy, D. Pantarotto, J.-P. Briand, S. Muller, M. Prato, A. Bianco, Nat Nano 2 (2007) 108.
[3] Y. Wenrong, T. Pall, J.J. Gooding, P.R. Simon, B. Filip, Nanotechnology 18 (2007) 412001.
[4] N. Sinha, J.T.W. Yeow, NanoBioscience, IEEE Transactions on 4 (2005) 180.
[5] D. Pantarotto, J.-P. Briand, M. Prato, A. Bianco, Chemical Communications (2004) 16.
[6] D. Pantarotto, R. Singh, D. McCarthy, M. Erhardt, J.-P. Briand, M. Prato, K. Kostarelos, A. Bianco, Angewandte Chemie 116 (2004) 5354.
[7] N.W.S. Kam, Z. Liu, H. Dai, Journal of the American Chemical Society 127 (2005) 12492.
[8] M. Foldvari, M. Bagonluri, Nanomedicine: Nanotechnology, Biology and Medicine 4 (2008) 183.
[9] C. Tripisciano, K. Kraemer, A. Taylor, E. Borowiak-Palen, Chemical Physics Letters 478 (2009) 200.
[10] G.R. Liu, Y. Cheng, D. Mi, Z.R. Li, International Journal of Modern Physics C 16 (2005) 1239.
[11] Y. Kang, Y.-C. Liu, Q. Wang, J.-W. Shen, T. Wu, W.-J. Guan, Biomaterials 30 (2009) 2807.
[12] K.T. Al-Jamal, H. Nerl, K.H. Muller, H. Ali-Boucetta, S. Li, P.D. Haynes, J.R. Jinschek, M. Prato, A. Bianco, K. Kostarelos, A.E. Porter, Nanoscale 3 (2011) 2627.
[13] A.E. Porter, M. Gass, J.S. Bendall, K. Muller, A. Goode, J.N. Skepper, P.A. Midgley, M. Welland, ACS Nano 3 (2009) 1485.
[14] A.E. Porter, M. Gass, K. Muller, J.N. Skepper, P.A. Midgley, M. Welland, Nat Nano 2 (2007) 713.
[15] F. Zhou, D. Xing, B. Wu, S. Wu, Z. Ou, W.R. Chen, Nano Letters 10 (2010) 1677.
[16] C. Lamprecht, I. Liashkovich, V. Neves, J. Danzberger, E. Heister, M. Rangl, H.M. Coley, J. McFadden, E. Flahaut, H.J. Gruber, P. Hinterdorfer, F. Kienberger, A. Ebner, Nanotechnology 20 (2009) 434001.
[17] V.K. Gangupomu, F.M. Capaldi, Journal of Nanomaterials 2011 (2011) 6.
[18] S. Höfinger, M. Melle-Franco, T. Gallo, A. Cantelli, M. Calvaresi, J.A.N.F. Gomes, F. Zerbetto, Biomaterials 32 (2011) 7079.

[19] P.N. Yaron, B.D. Holt, P.A. Short, M. Losche, M.F. Islam, K.N.J. Dahl, J. Nanobiotechnology 9 (2011) 45.
[20] V. Raffa, G. Ciofani, O. Vittorio, C. Riggio, A. Cuschieri, Nanomedicine 5 (2009) 89.
[21] R. Parthasarathi, N.R. Tummala, A. Striolo, The Journal of Physical Chemistry B 116 (2012) 12769.
[22] Y. Tu, M. Lv, P. Xiu, T. Huynh, M. Zhang, M. Castelli, Z. Liu, Q. Huang, C. Fan, H. Fang, R. Zhou, Nat Nano 8 (2013) 594.
[23] C.F. Lopez, S.O. Nielsen, P.B. Moore, M.L. Klein, Proceedings of the National Academy of Sciences of the United States of America 101 (2004) 4431.
[24] R. DeVane, A. Jusufi, W. Shinoda, C.-c. Chiu, S.O. Nielsen, P.B. Moore, M.L. Klein, The Journal of Physical Chemistry B 114 (2010) 16364.
[25] J. Wong-Ekkabut, S. Baoukina, W. Triampo, I.M. Tang, D.P. Tieleman, L. Monticelli, Nat Nano 3 (2008) 363.
[26] S. Pogodin, V.A. Baulin, ACS Nano 4 (2010) 5293.
[27] M. Lelimousin, M.S.P. Sansom, Small (2013) n/a.
[28] S. Baoukina, L. Monticelli, D.P. Tieleman, The Journal of Physical Chemistry B 117 (2013) 12113.
[29] A. Magrez, S. Kasas, V. Salicio, N. Pasquier, J.W. Seo, M. Celio, S. Catsicas, B. Schwaller, L. Forró, Nano Letters 6 (2006) 1121.
[30] G. Milano, T. Kawakatsu, Journal of Chemical Physics 130 (2009) 214106.
[31] K.M. Langner, G.J.A. Sevink, Soft Matter 8 (2012) 5102.
[32] M. Mueller, K. Katasov, M. Schick, Physics Reports 434 (2006) 113.
[33] G. Milano, T. Kawakatsu, A. De Nicola, Physical Biology 10 (2013) 045007.
[34] M. Homberg, M. Muller, The Journal of Chemical Physics 132 (2010) 155104.
[35] G.J.A. Sevink, M. Charlaganov, J.G.E.M. Fraaije, Soft Matter 9 (2013) 2816.
[36] K.C. Daoulas, M. Muller, J. Chem. Phys. 125 (2006).
[37] K.C. Daoulas, M. Muller, J.J. de Pablo, P.F. Nealey, G.D. Smith, Soft Matter 2 (2006) 573.
[38] G. Milano, T. Kawakatsu, Journal of Chemical Physics 133 (2010) 214102.
[39] A. De Nicola, Y. Zhao, T. Kawakatsu, D. Roccatano, G. Milano, Journal of Chemical Theory and Computation 7 (2011) 2947.
[40] A. De Nicola, Y. Zhao, T. Kawakatsu, D. Roccatano, G. Milano, Theoretical Chemistry Accounts 131 (2012) 1167.
[41] Y. Zhao, A. De Nicola, T. Kawakatsu, G. Milano, Journal of Computational Chemistry 33 (2012) 868.

**Figure and Tables**

(1.5 COLUMN)

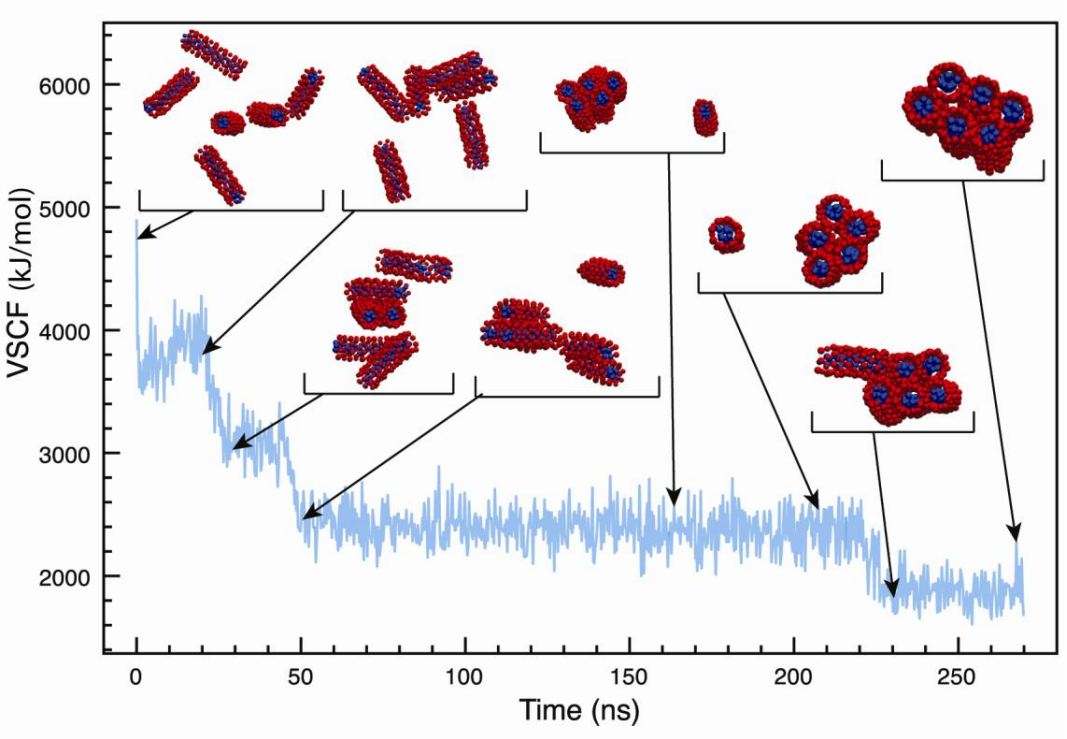


**Figure 1.** Time evolution of particle-field potential (first addend of eq. 2 of the supporting material) togheter with some snapshots.

(SINGLE COLUMN)

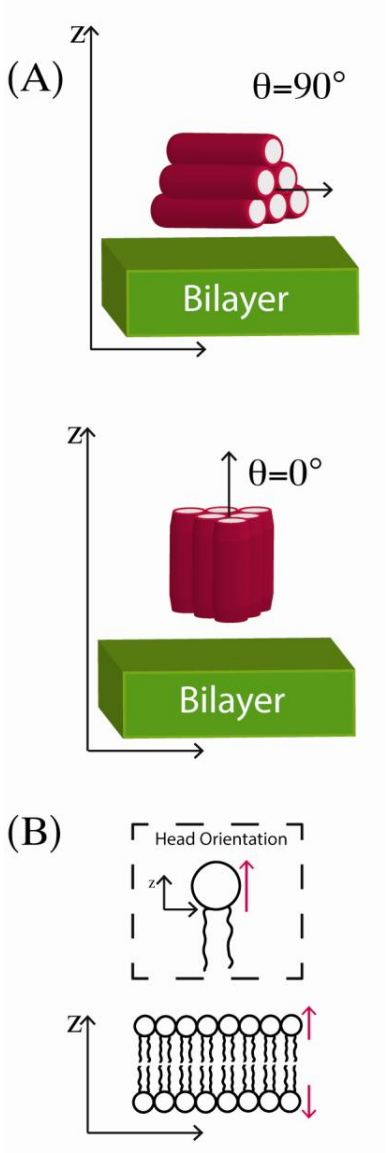


**Figure 2.** Definition of: (A) CNT bundle orientation with respect to the lipid bilayer plane. (B) orientation of lipid molecules with respect to the bilayer plane. A vector (depicted in red) joining beads of type G and N (the bead definition is reported in a previous paper at the ref. 38) is used to define the orientation along the *z* axis.

(2 COLUMNS)

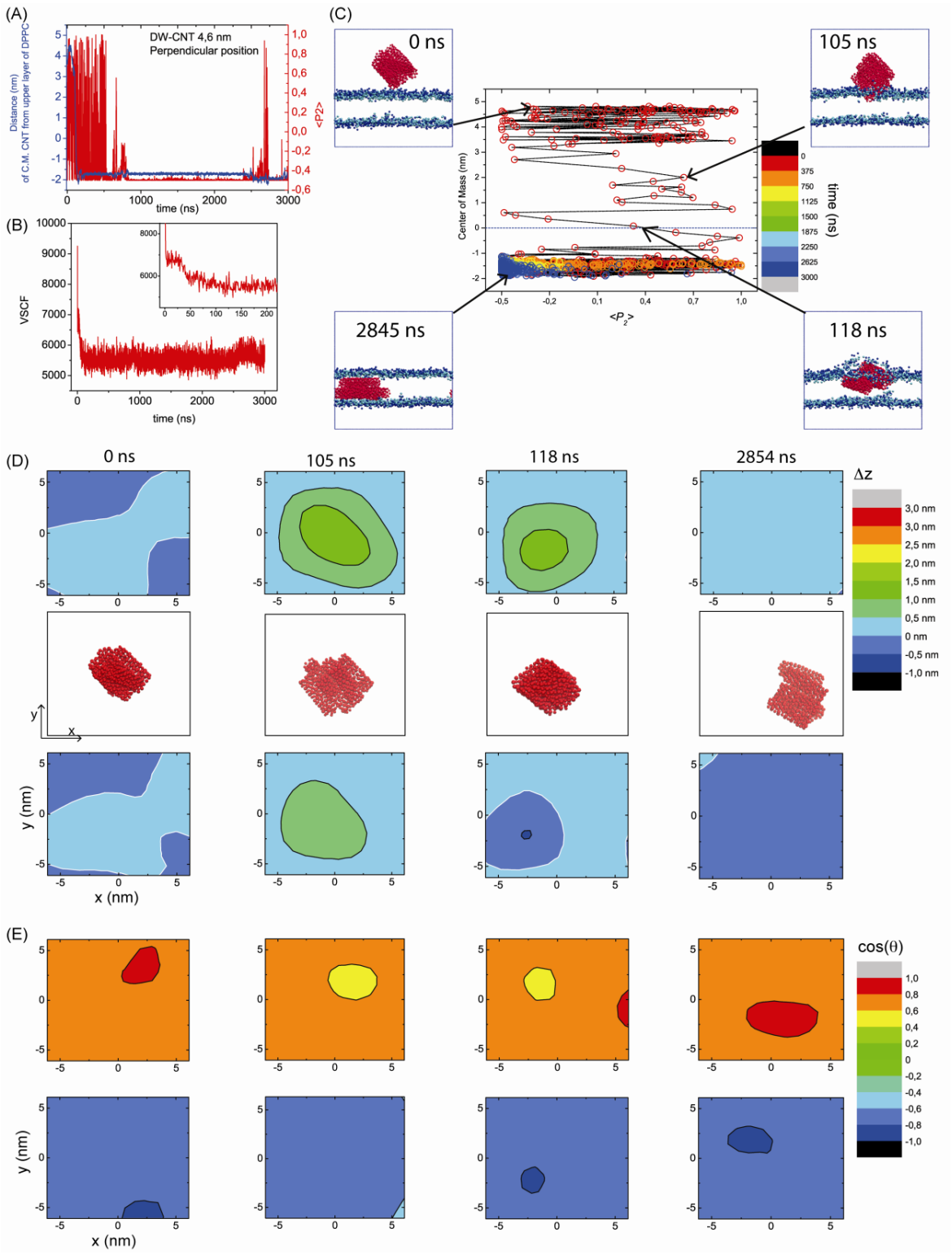


**Figure 3.** System II: Time behavior of (A) CNT bundle center of mass height (blue curve) and orientation ($P_2$, red curve); (B) Particle field potential; (C) correlation between center of mass height and bundle orientation together with some snapshots of the system; (D) Deviation ($\Delta z$ ) from the equilibrium height for upper (top of figure) and lower lipid layers (bottom of figure) for different configurations In the center of figure D the corresponding configurations of CNT bundle

are depicted. (E) Lipid orientation $\cos\theta$. Both $\Delta z$ and $\cos\theta$ have been averaged on a lattice made of 8x8 cells. In every cell, on average, there are 6.5 lipids/layer.

(SINGLE COLUMN)

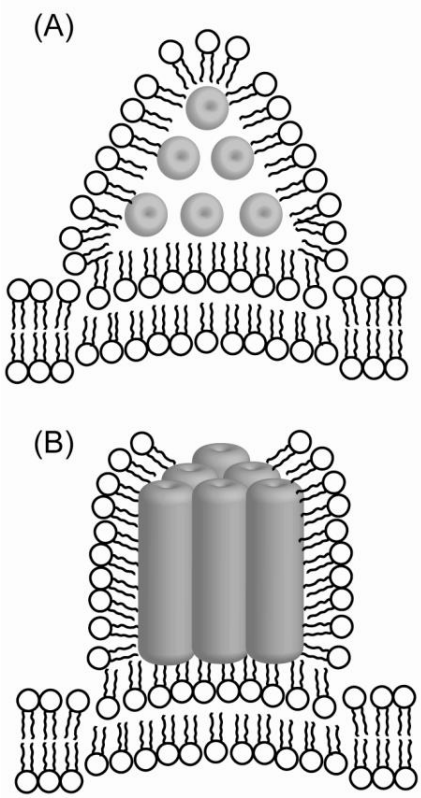


**Figure 4** Typical orientations of lipids during the insertion process of a CNT bundle in parallel (A) and perpendicular (B) orientation with respect to the bilayer plane.

(2 COLUMNS)

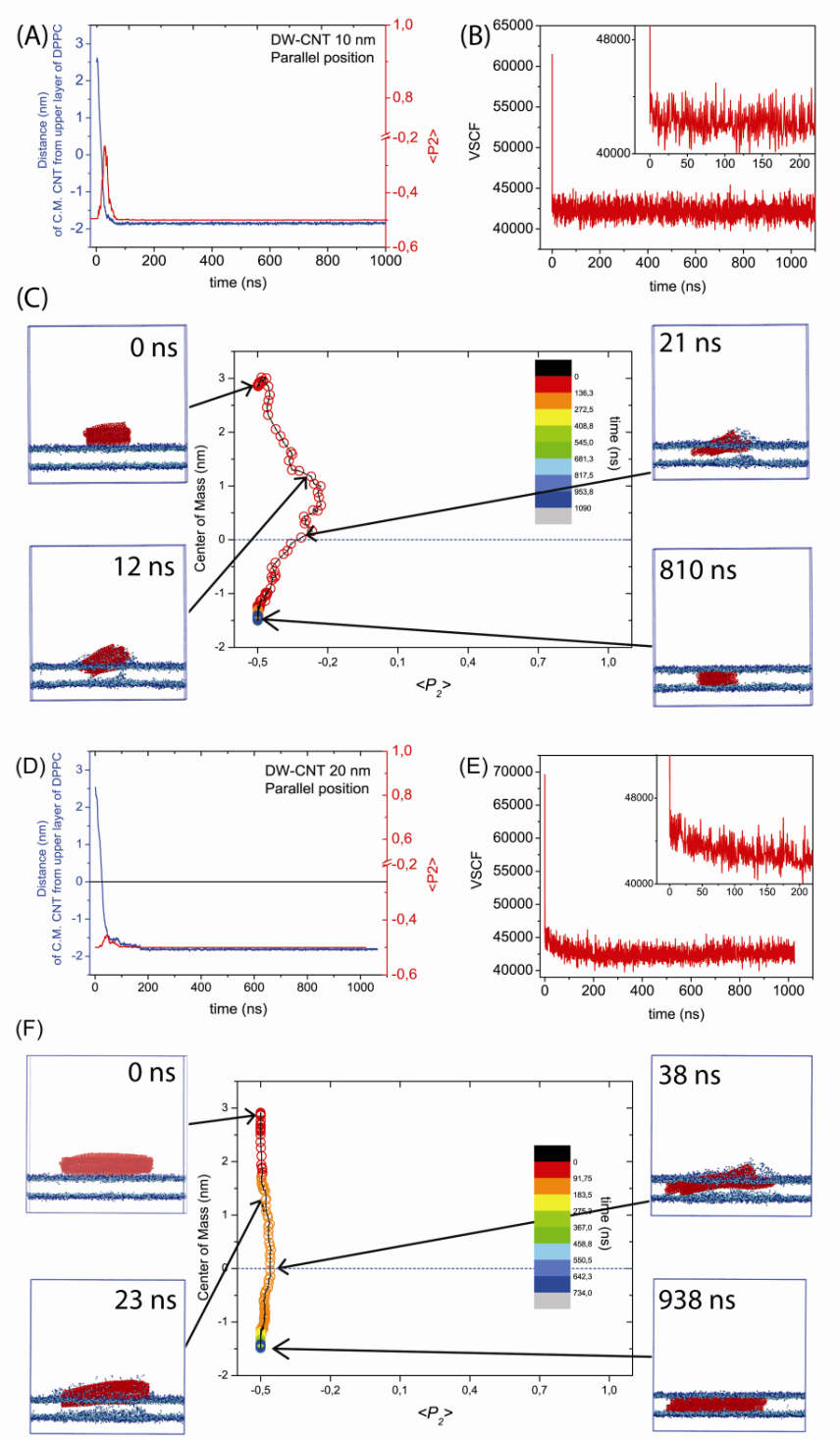


**Figure 5.** Bundle in parallel orientation: System III (A-B-C). Time behavior of (A) DWCNT-10nm bundle center of mass height (blue curve) and orientation ($P_2$, red curve); (B) Particle field potential; **(**C) correlation between center of mass height and bundle orientation together with some snapshots. System IV (D-E-F). Time behavior of (D) DWCNT-20nm bundle center of mass height and orientation; (E) Particle field potential. **(**F) correlation between center of mass height and bundle orientation together with some snapshots.

(2 COLUMNS)

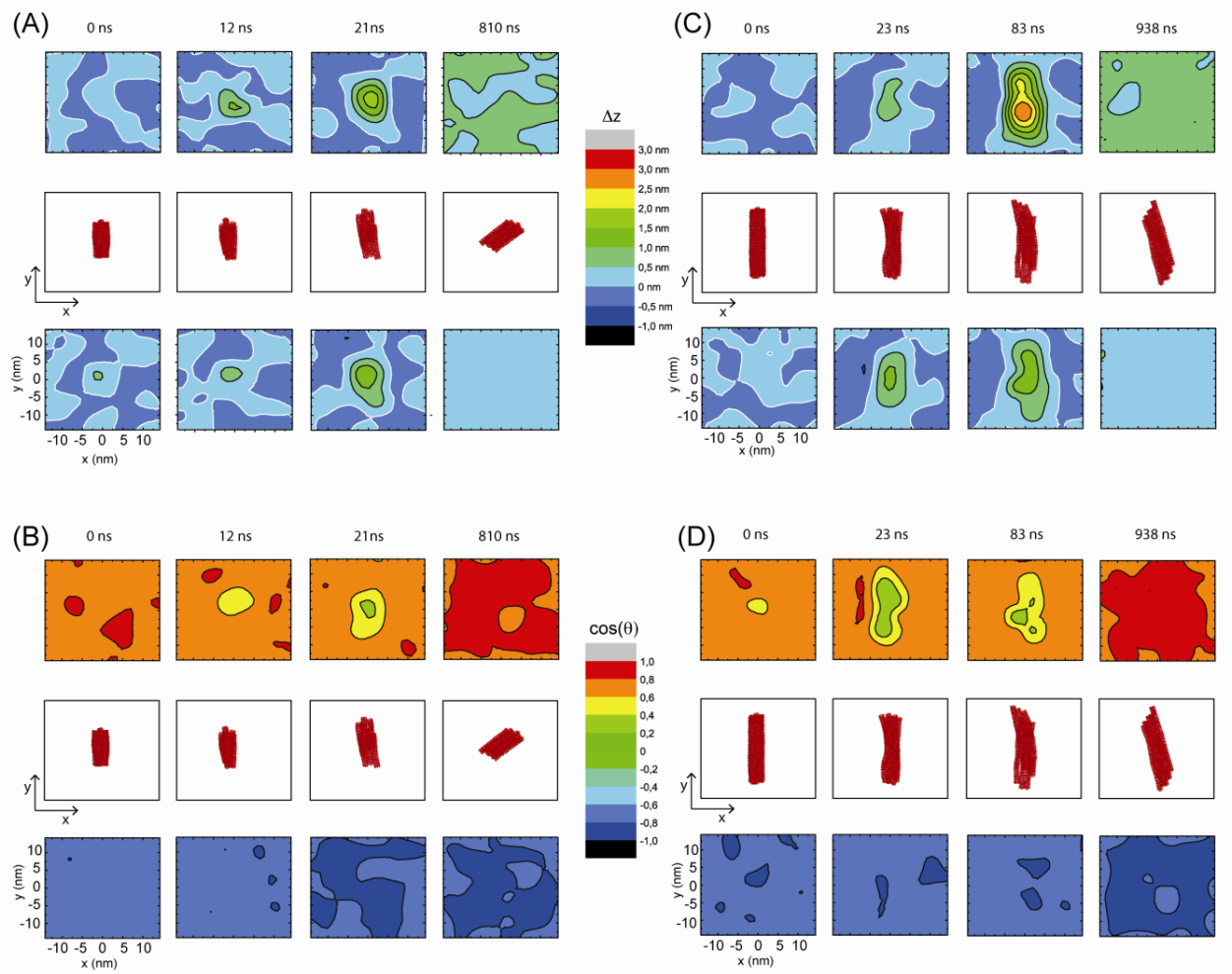


**Figure 6.** Deviation $\Delta z$ (A, C) and Lipid orientation $\cos\theta$ for the systems III and IV with bundle CNT in parallel orientation. (A) deviation $\Delta z$ from the equilibrium height for upper (top of the panel) and lower lipid layers (bottom panel) for different configurations of system III. (C) Deviation $\Delta z$ for system IV. (B) Lipid orientation $\cos\theta$ for system III. (D) Lipid orientation $\cos\theta$ for system IV. In the center of each figure A, B, C and D, the corresponding configurations of CNT bundle are depicted. Both $\Delta z$ and $\cos\theta$ have been averaged on a lattice made of 16x16 cells (with the same cell size, about 2 nm, of the system II). In every cell, on average, there are 6.5 lipids/layer.

(2 COLUMNS)

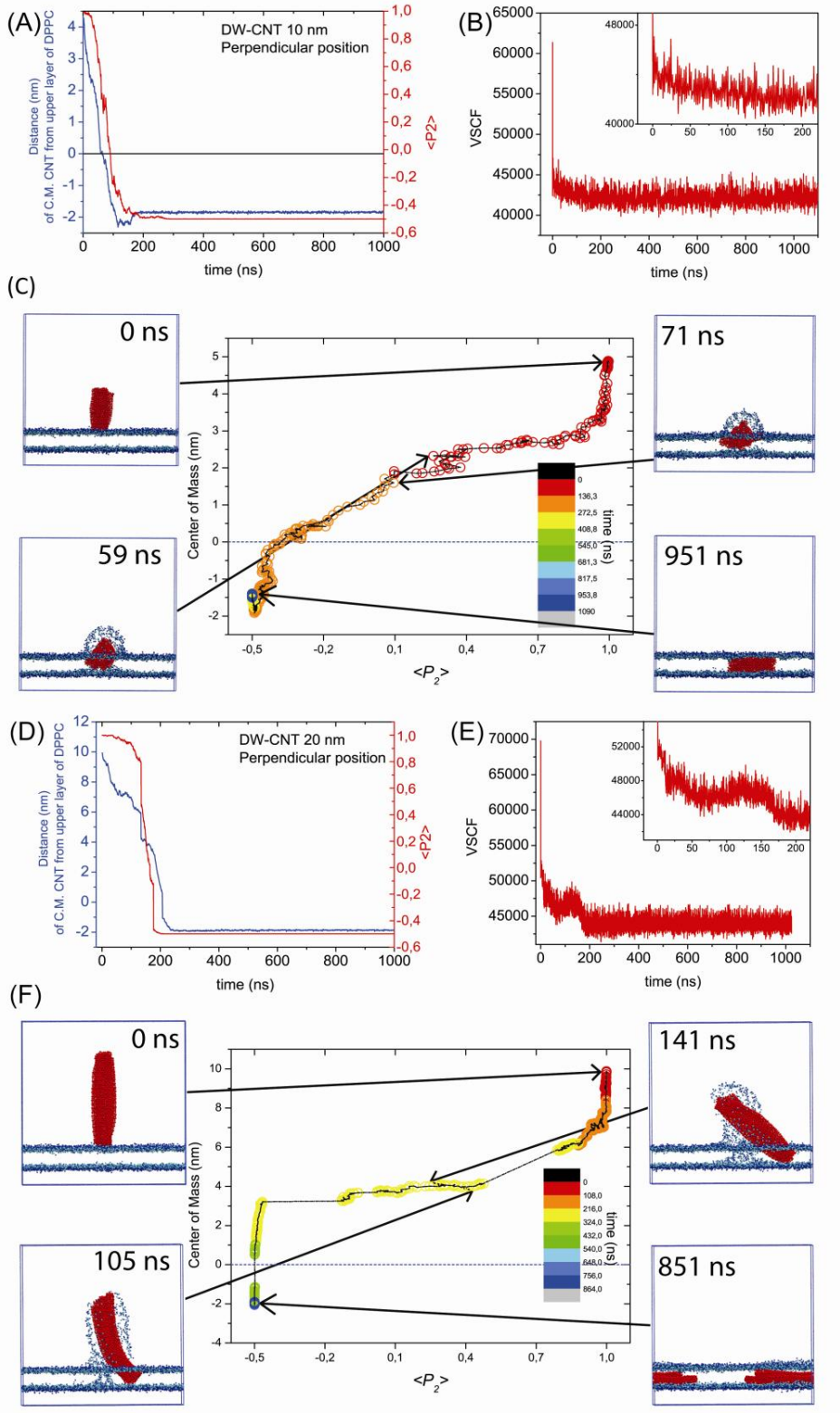


**Figure 7.** Bundle in perpendicular orientation: System III (A-B-C). Time behavior of (A) DWCNT-10nm bundle center of mass height (blue curve) and orientation ($P_2$, red curve); (B) Particle field potential; **(**C) correlation between center of mass height and bundle orientation together with some snapshots. System IV (D-E-F). Time behavior of (D) DWCNT-20nm bundle center of mass height

and orientation; (E) Particle field potential. **(**F) correlation between center of mass height and bundle orientation together with some snapshots.

(2 COLUMNS)

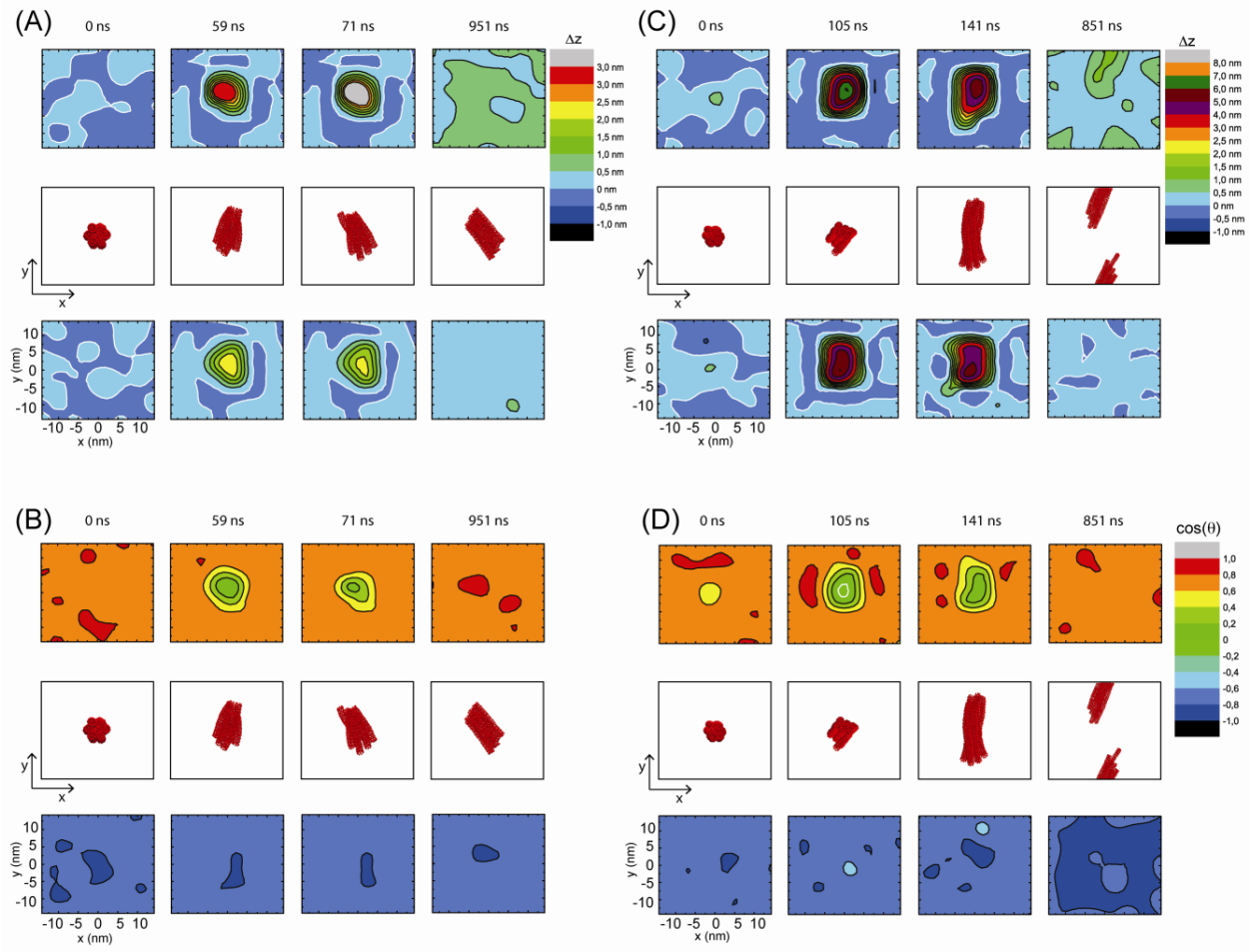


**Figure 8.** Deviation $\Delta z$ (A, C) and Lipid orientation $\cos\theta$ for the systems III and IV with bundle CNT in perpendicular orientation. (A) deviation $\Delta z$ from the equilibrium height for upper (top of the panel) and lower lipid layers (bottom panel) for different configurations of system III. (C) Deviation $\Delta z$ for system IV. (B) Lipid orientation $\cos\theta$ for system III. (D) Lipid orientation $\cos\theta$ for system IV. In the center of each figure A, B, C and D, the corresponding configurations of CNT bundle are depicted. Both $\Delta z$ and $\cos\theta$ have been averaged on a lattice made of 16x16 cells (with the same cell size, about 2 nm, of the system II). In every cell, on average, there are 6.5 lipids/layer.

(2 COLUMNS)

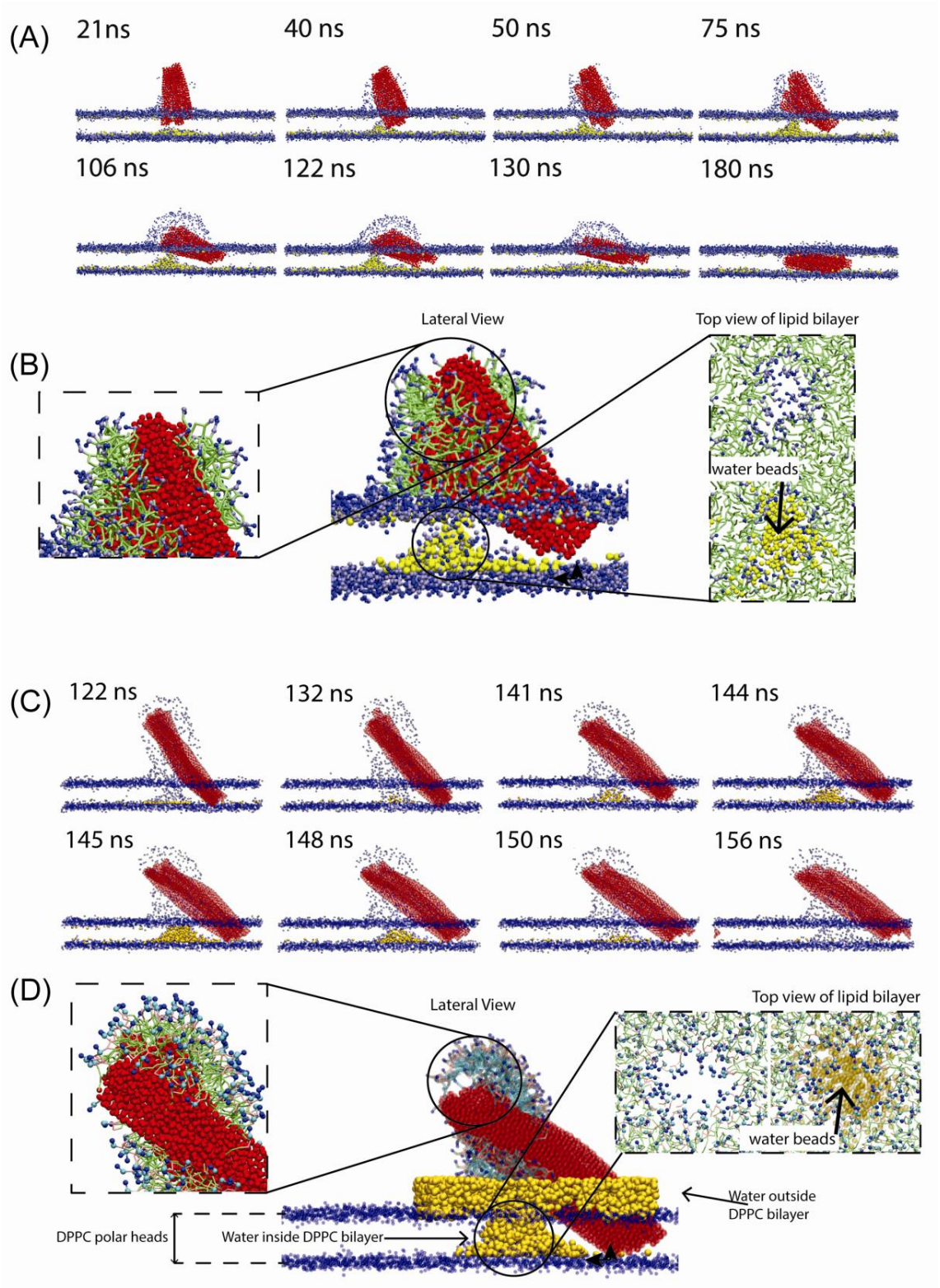


**Figure 9.** Process of pore formation inside the lipid bilayer during the insertion process of a bundle made of CNTs long 10 nm (A) and 20 nm (C). The lipid orientations corresponding to micelle in

water around the CNTs (inset on the left side) and reverse micelle (around the pore including water) aggregates (right side) are highlighted for both bundles lengths: (B) 10 nm, (D) 20 nm.

Table 1 – Systems Composition

| System | Box length [$x$=$y$=$z$] (nm) | DWCNT Length (nm) | No. of DPPC | No. of CG-water Beads* | No. of DWCNT | Total No. of Particles | Simulation time (μs) |
|---|---|---|---|---|---|---|---|
| I | 12.0000 | 4.6 | - | 14051 | 6 | 14844 | 0.27 |
| II | 16.3521 | 4.6 | 832 | 27829 | 6 | 38605 | 3.0 |
| III | 32.7042 | 10.0 | 3319 | 267088 | 6 | 308500 | 1.2 |
| IV | 32.7042 | 20.0 | 3319 | 265541 | 6 | 308537 | 1.2 |

* A single CG water bead corresponds to 4 real water molecules.

**Supplementary Materials**

**Click here to download Supplementary Materials: supporting_material.docx**